

Segmentation and Characterization of Macerated Fibers and Vessels Using Deep Learning

Saqib Qamar^{1,2}, Abu Imran Baba³, Stéphane Verger^{2,3,4*},
Magnus Andersson^{1,2,5*}

¹Department of Physics, Umeå University, Umeå, 90187, Sweden.

²Integrated Science Lab, Department of Physics, Umeå University, Umeå, 90187, Sweden.

³Umeå Plant Science Centre (UPSC), Department of Forest Genetics and Plant Physiology, Swedish University of Agricultural Sciences, Umeå, 90183, Sweden.

⁴Umeå Plant Science Centre (UPSC), Department of Plant Physiology Umeå University, Umeå, 90187, Sweden.

⁵Umeå Centre for Microbial Research (UCMR) Umeå University, Umeå, 90187, Sweden.

*Corresponding author(s). E-mail(s): stephane.verger@umu.se;
magnus.andersson@umu.se;

Contributing authors: saqib.qamar@umu.se; abu.baba@slu.se;

Abstract

Purpose: Wood comprises different cell types, such as fibers and vessels, defining its properties. Studying their shape, size, and arrangement in microscopic images is crucial for understanding wood samples. Typically, this involves macerating (soaking) samples in a solution to separate cells, then spreading them on slides for imaging with a microscope that covers a wide area, capturing thousands of cells. However, these cells often cluster and overlap in images, making the segmentation difficult and time-consuming using standard image-processing methods. **Results:** In this work, we develop an automatic deep learning segmentation approach that utilizes the one-stage YOLOv8 model for fast and accurate fiber and vessel segmentation and characterization in microscopy images. The model can analyze 32640 x 25920 pixels images and demonstrate effective cell detection and segmentation, achieving a mAP_{0.5–0.95} of 78 %. To assess the model's robustness, we examined fibers from a genetically modified tree line known for longer fibers. The outcomes were comparable to previous manual measurements. Additionally,

we created a user-friendly web application for image analysis and provided the code for use on Google Colab. **Conclusion:** By leveraging YOLOv8’s advances, this work provides a deep learning solution to enable efficient quantification and analysis of wood cells suitable for practical applications.

Keywords: Instance segmentation, YOLO, composites, soaking, optical microscopy

1 Introduction

Fiber cells are the main constituent of wood. These fibers provide the wood with mechanical strength to resist external sources of mechanical stress such as wind. They are also crucial to allow and support the growth in the height of the trees [1]. But more importantly, they have a high economic importance as they are the basic constituent of most of the wood derived products. Wood fibers are extracted by pulping, which separates these cells into independent fiber cells. They can then be reassembled as paper, and fibers are increasingly used in applications such as in bio-composites, smart papers, and new packaging and materials. In addition to fibers, wood comprises vessels, that together with the fibers generally determine the characteristics of wood [2]. Nevertheless, one key factor for wood quality is the fiber length that can serve in fiber-based products. Yet, we still know very little about how these fibers develop and elongate and the genetic determinants that regulate fiber length. With this knowledge, fiber properties could be improved to produce better and stronger wood for construction and fiber-based products in more sustainable production systems. The demand for renewable fiber-based products is constantly increasing as we move away from fossil resources-based products, thus we need to establish better tools to study fiber length in a very robust and high-throughput manner.

A classical method to study wood fiber length consists of macerating (soaking) wood samples in a solution that separates individual cells [3]. Cells suspended in liquid solutions can be transferred onto microscopy slides for examination. Once prepared, these slides can be observed using a standard light microscope. The images captured can then be analyzed using image processing software like ImageJ, which allows for the manual measurement of individual fiber lengths [4]. This task is, however, highly time-consuming and prone to user bias and errors during the manual measurement step. Overall, this highly limits the throughput of this type of analysis. Alternatively, it is possible to use so-called fiber analyzers. These machines allow the high throughput image acquisition of fibers floating in a constantly stirred solution, generating high-speed and unbiased measurements [5]. However, the resolution of data acquisition is often limited, and it can be difficult to differentiate individual fibers from clumps of fibers that have not been properly detached from each other. While this may not be a limitation for industrial applications, it can become limiting when it comes to accurately studying the biology of fibers and their individual length, width, and other shape descriptors. This type of equipment can also be very costly and is not widely available to many research labs contrary to light microscopes, even those equipped with a motorized stage. A more appropriate solution for fundamental research application

may thus be to make use of commonly available light microscopes equipped with motorized stages to acquire large fields of view of wood macerates mounted between slides and cover-slips. This can then be coupled with new image processing technologies to automate the time-consuming task of identifying and measuring fiber cells in those high-resolution images.

While most recent light microscopes are equipped with motorized stages and the capacity to automatically generate large stitched images, the remaining limiting step is the image processing for the detection (segmentation) and shape analysis of the fibers. Several studies have developed image processing methods to analyze fibers from wood section images [6–12]. However, most of these methods are only adapted for images from cross-sections of wood samples. These samples are typically prepared in a transverse orientation. Although this method provides crucial information about certain aspects of cell arrangement and wood density, it does not directly yield information about the length of fiber cells. Those images are also less challenging for classical image segmentation tasks, as individual cells in the images do not overlap. As such, the image can be divided into regions (e.g., individual cells and background) where each pixel is only assigned to one cell or region. On the other hand, 2D images obtained from wood macerates contain many fibers that frequently overlap. In turn, many pixels in the image can belong to more than one cell of interest. This is challenging because most existing segmentation algorithms, such as thresholding, watershed, and even most machine learning and deep learning approaches, do not handle this type of case when solving segmentation tasks.

Deep learning is a type of machine learning that has been very successful in image and language tasks [13–18]. Deep learning uses neural networks called deep neural networks (DNNs) that are trained on large amounts of data to perform a task directly without needing human-designed features [19]. Convolutional neural networks (CNNs) are a type of deep neural network well-suited for processing images [20]. CNNs apply a series of filters to the input to automatically learn and extract useful features from the images [21]. This removes the need for humans to design feature extractors manually. CNNs have been widely used for image segmentation [22, 23], including for segmenting cells in microscope images in biomedicine [24, 25]. Because in our images of wood macerates, cells often overlap, we need a neural network architecture that allows object detection and that could thus fully identify individually crossing and overlapping cells rather than simply splitting the image into regions. This makes instance segmentation the best approach since it identifies each individual cell and assigns pixels to the appropriate cell instance. Popular existing instance segmentation methods such as Faster R-CNN [26], Mask R-CNN [27], and RetinaNet [28] have been successfully applied to cellular image segmentation [29–31]. These methods use deep convolutional neural networks (CNNs) like VGG [32] and ResNet [33] to extract features from the input images. They rely on anchors, which are predefined bounding boxes of certain shapes and sizes tiled across the image, to detect multiple overlapping cells. Multiple anchors are assigned to each pixel. Based on the extracted features, the network then predicts the probability that each anchor contains a cell. Non-maximum suppression (NMS) [34] selects the anchors with the highest probabilities as the final cell detections. However, these two-stage methods are slow for inference. One-stage methods

such as Single Shot MultiBox Detector (SSD) [35] and You Only Look Once (YOLO) series streamline object detection by simultaneously predicting object locations and class probabilities in a single pass. This approach significantly enhances the speed of inference compared to multi-stage processes. Among one-stage models, YOLO offers a good balance of speed and accuracy for real-time applications. Given that wood images often feature numerous overlapping cells, we propose that the YOLO algorithm is particularly well-suited for addressing this challenge.

In this paper, we develop a YOLOv8 [36] based model to segment and classify fiber and vessel cells from 2D microscopy images. We initially created a new dataset consisting of wood macerate samples and their images. This dataset includes 3850 images, which encompass 28 358 individual fibers and 1502 individual vessels. Each of these was manually annotated to retrain the YOLOv8 model. Subsequently, we demonstrate that the retrained YOLOv8 model achieves rapid inference speeds while maintaining high accuracy in identifying and classifying individual vessels and fibers. Furthermore, the model proves highly efficient even when processing large tiled images (32 640 x 25 920). To facilitate the use of this retrained model, we developed a browser-based interface. This interface, accessible after local installation, enables users to upload images via drag and drop. The system then provides measurements of the fibers and vessels, including their length, width, and area. Additionally, users can access the training and prediction code run on Google Colab [37] in the GitHub repository [38]. Lastly, to validate the effectiveness of our new methods, we applied them to a well-known poplar transgenic line, which is recognized for having distinctly longer wood fibers than its wild-type relative. This approach aimed to corroborate previous manual measurements of fiber length differences in these lines.

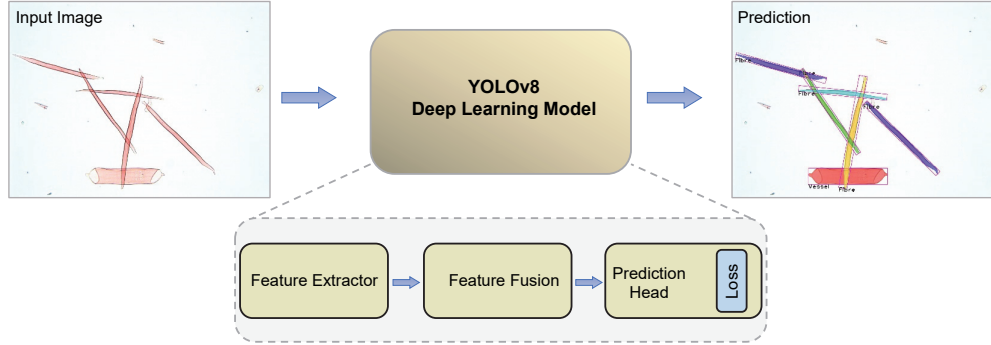


Fig. 1 Schematic of the YOLOv8 architecture for fiber and vessel segmentation. The model contains a Feature Extractor for feature extraction, Feature Fusion for feature aggregation, Prediction Head for predicting the objects’ bounding boxes, classes, and masks. The loss component is used to optimize the model performance. An input image is passed through the network, which performs classification, detection, and segmentation jointly. This enables the delineation of individual cells even when overlapping, as shown in the prediction output.

2 Image capturing method

2.1 Sample preparation

Stem samples from approximately 3-month-old greenhouse-grown hybrid aspen (*Populus tremula* L. \times *tremuloides* Michx.) clone T89 were collected between internodes above 10 centimeters from the soil. Initially, the bark was removed from these stem segments and then the equal size of the xylem region was trimmed from these wood samples starting (2-3 mm) after the cambium region to macerate them into individual vessels and fiber cells. Maceration was performed on xylem wood samples by immersing them in maceration solution (30% Hydrogen peroxide: glacial acetic acid, 2:1 v/v) and heating at 90°C with periodic shaking for 5 hours, as previously described in [3]. The macerated solution was then sedimented by low-speed centrifugation (1500 rpm), washed a few times with water, and imaged immediately with a microscope.

3-month-old greenhouse transgenic trees overexpressing the *GA20ox1* gene "Arabidopsis gibberellin 20-oxidase" (Ara GA20ox1 Line 1A) [5] were used with their respective controls as T89. The stem segments from 3-3 trees each from the overexpressing line and wild type T89 were sampled, macerated, stained, and finally imaged with similar conditions or parameters as described above. Four 361-tile stitched images (containing fibers and vessels) were obtained from the trimmed stem samples of each of these trees for both the control and overexpression line.

2.2 Imaging

A few drops from the obtained macerated solution were first stained with the safranin solution (1 %) that stains lignified tissues in xylem cells. Then, the samples were imaged on a glass slide using a Leica DMI8 inverted microscope in brightfield mode with transmitted white light (Leica Microsystems, Germany). Individual images were acquired using a 10X objective lens and DFC7000T color camera with a pixel size of 4.54 μm and a resolution of 1920 x 1440. Tile images made of 19 x 19 (361) individual images were acquired with the Navigator function of the microscope using a 10 % overlap. Tile images were merged by the LAS X software (Leica Microsystems, Germany).

2.3 Statistics

We used a t-test statistical method to validate whether the trained model outputs consistent results across different image groups. Specifically, we tested for scale invariance by running the model on different-sized crops from the same large images. We also compared model predictions on an overexpression line GA20ox 1A and wildtype T89 as control. The t-statistic is calculated as $t = \frac{(\bar{X}_1 - \bar{X}_2)}{\text{SED}}$, where \bar{X}_1 and \bar{X}_2 are the sample means and SED is the standard error of the difference between the means. We employed Scipy's *ttest_ind()* to automatically compare two independent data samples, assessing significant mean differences based on t-test assumptions.

3 Computational Method

3.1 Images annotation and dataset preparation

To identify fibers and vessels in microscope images, we created a dataset of over 1300 individual images showing these structures in different shapes and sizes. The images are 1920 x 1440 pixels in size. We carefully outlined the fibers and vessels in each image using the VGG Image Annotator [39]. This created a ground truth or guide to the actual fibers and vessels in the images. The outlines were saved as JSON files, which store the coordinates of the polygons drawn around each object, which can be seen in Fig. S1. We resized the large images into smaller 1024 x 1024 pixel images to avoid running out of memory on our graphics card. We also used data augmentation techniques to increase the number of training images. For example, by applying transformations like rotating, scaling, and flipping the original images, we created more variety in the dataset. This also helps the machine learning model learn robust features that apply to new images. From 1300 original images, we generated 3850 augmented images with around 29 861 annotated objects.

To train the YOLO model, we randomly split the dataset into training (85%) and validation (15%) sets. The training data is used to update the model’s parameters. The validation data is used to evaluate the model during training but not to update parameters. This split helps prevent overfitting and ensures the model generalizes well.

3.2 Deep learning approach

We used the YOLOv8-seg deep learning method, which is a variant of YOLOv8 architecture designed explicitly, for instance, segmentation tasks [36]. During the model training process, we utilized the pre-trained YOLOv8 model on the COCO val2017 dataset as a starting point. The architecture of the YOLOv8 algorithm consists of four main components: feature extractor, feature fusion, prediction head, and loss function. The components are shown in Fig. 1 and with more details in Fig. S2. Here, we look into the design concepts of each architecture module.

The feature extractor is the first part of the model and is responsible for extracting features at different stages from the input image. The output features from the different stages have different spatial resolutions. The earlier stages of the feature extractor network extract low-level features such as edges and corners. The later stages extract high-level features such as object shapes and parts. The feature extractor down-samples the input image because it extracts features at later stages.

The feature fusion module combines the output features from different stages of the feature extractor network to form a unified representation of the image. Deep neural networks capture increasingly detailed features as the network becomes deeper, which improves object prediction. However, as the network depth increases, the object localization accuracy for detecting small objects decreases owing to excessive convolution operations, resulting in the loss of important information. To address this tradeoff, the feature fusion module incorporates a multi-scale fusion of features using architectures such as a Feature Pyramid Network (FPN) and Path Aggregation Network (PAN).

The feature fusion module performs different operations to extract higher-level features from the input features and consolidate the outputs from various stages of the feature extractor into a single representation. This unified representation enhances the object detection and segmentation performance.

The prediction-head module transforms the encoded image features into usable predictions for object detection and segmentation. This makes the final predictions based on the consolidated representation from the feature-fusion module. The head module combines features from earlier modules and leverages them to predict bounding boxes, classes, and masks for the objects in the image. By dividing the prediction into specialized branches, it efficiently performed classification, localization, and masking in a coordinated manner. The prediction head is the final component that outputs the actual detections and segmentations after processing using the complete YOLOv8 architecture.

The loss function in YOLOv8 measures how accurately the model detects and segments objects. It compares the model predictions with the ground-truth labels. The loss function is used to train the model to improve its performance. YOLOv8 has separate branches for classification, bounding-box regression, and masking. For classification and masking, the cross-entropy loss was used to minimize errors. Bounding box detection uses two losses: distributed focal loss (DFL) and CIOU Loss. These consider the aspect ratio between the predicted and ground-truth boxes. The overall loss is the sum of the losses from different branches. A lower loss indicates that the model is more accurate at detecting, classifying, and segmenting objects. Loss guides model training to improve these areas. The detailed layer-wise architecture is illustrated in Fig. S2.

3.3 Measuring the morphology of objects

To accurately measure the morphological traits of objects detected in images, we utilize a combination of deep learning-based instance segmentation prediction and traditional image processing techniques. Specifically, we leverage the YOLOv8 model to identify and localize objects of interest within images, predicting bounding boxes and contours around each instance. However, the predicted bounding boxes may not tightly envelop the objects. To enable more precise morphological measurement, we integrate functions from the OpenCV computer vision library to further analyze the object contours [40].

Once YOLOv8 predicts axis-aligned bounding boxes and contours of detected objects, we calculate a minimum area bounding rectangle that encloses all the contour points using OpenCV’s `cv2.minAreaRect()` built-in function. This rotated rectangle fits the object contour much more tightly than the original bounding box. We extract the coordinates of the four corners of this rectangle using `cv2.boxPoints()`. This gives us a precise measurement of the object’s length and width based on the rectangle side lengths. The longer side is taken as the length of the object, while the shorter side corresponds to the width. Pixel distances are converted to real-world units by multiplying with a scale factor depending on the microscopy resolution.

In addition to length and width, we leverage OpenCV’s `cv2.contourArea()` method to accurately measure the area enclosed within the detected contours. This gives

a more precise estimate of object area than simply using the bounding box area. The object detection model’s bounding boxes provide a good initial localization, but contour analysis gives significantly more accurate morphological measurements. A schematic diagram showing the concept is shown in Fig. 2, where each grid cell represents a pixel point. The corner points of the rotated rectangle that fits with the minimum area on detected contours of objects are denoted as P1(x1, y1), P2(x2, y2), P3(x3, y3), and P4(x4, y4). a and b refer to the number of pixels in the detection box’s length and width, respectively, calculated using Eq. 1 and 2. The object’s length is determined by selecting the highest value between the two parameters a and b . Finally, the average width is calculated by dividing the object area by the length.

$$a = \sqrt{(x1 - x2)^2 + (y1 - y2)^2}. \quad (1)$$

$$b = \sqrt{(x2 - x3)^2 + (y2 - y3)^2}. \quad (2)$$

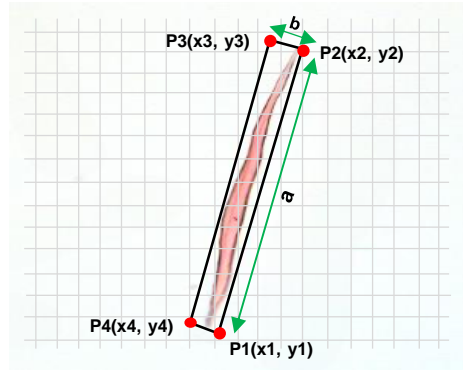


Fig. 2 Example of a segmented fiber and the corresponding image analysis that automatically measures the object’s morphological traits.

Table 1 The table compares YOLOv8m-seg, YOLOv8l-seg, and YOLOv8x-seg models trained on our generated dataset using both SGD and Adam optimizers.

Model	Optimizer	Best Epoch	mAP 50	mAP 50-95	Speed GPU V100 (ms)
YOLOv8m-seg	SGD	466	0.93	0.73	7.9
	Adam	486	0.95	0.75	8.0
YOLOv8l-seg	SGD	452	0.93	0.75	16.2
	Adam	505	0.94	0.76	15.7
YOLOv8x-seg	SGD	576	0.93	0.76	21.4
	Adam	591	0.95	0.78	20.9

4 Experimental setup

4.1 YOLOv8 model retraining and hyperparameter tuning with wood macerate dataset

During the training process of all models, we utilized pre-trained YOLOv8 models on the COCO val2017 dataset as a starting point. To train the YOLO model, we use 3350 images for training and 500 images for validation. The training data is used to update the model’s parameters. The validation data is used to evaluate the model during training but not to update parameters. We have used YOLOv8-m, l, and x in our experiment. YOLOv8-m uses a medium-sized feature extractor and more feature fusion levels, YOLOv8-l utilizes a larger feature extractor and most feature fusion levels compared to YOLOv8-m, and YOLOv8-x uses an even larger feature extractor and more feature fusion compared to YOLOv8-l. We find the convergence level and best optimizer for these models during training. Based on experimental data from Ultralytics, we observed that YOLOv5 training required 300 epochs, while YOLOv8 training increased the number of epochs to 600. Initially, we set the number of epochs to 600 and incorporated a patience value of 50. This means that if no noticeable improvement occurred after waiting for 50 epochs, the training would terminate early. However, during the training of YOLOv8m, we found that the model reached its best performance at epoch 486 and training stopped early at epoch 534.

We chose hyperparameters for model training as suggested in reference [41]. The selection of an appropriate optimization algorithm is crucial when training YOLOv8-seg. The optimizer determines how the model parameters are updated during training to minimize the loss function. For small custom datasets, the Adam (Adaptive Moment Estimation) optimizer is recommended, while the SGD (Stochastic Gradient Descent) optimizer tends to perform better on larger datasets. Consequently, we trained YOLOv8-seg models separately using the Adam and SGD optimizers. The results of comparing the effects of these two optimizers on model training are presented in Table 1.

We opted for the Adam optimizer with a weight decay of 5×10^{-4} and an initial learning rate of 1×10^{-3} . Furthermore, we set the input image size to 1024 and trained the different models using a TITAN V100 16GB with a batch size of 8. The models were trained on Python 3.8 and PyTorch 1.10.0. We recommend using Python 3.7 or higher and PyTorch 1.7 or higher for training. It is important to note that utilizing GPUs with more significant memory and higher computational power can significantly enhance the speed of model training.

4.2 Evaluation metrics

To evaluate the performance of the models, we use four metrics: precision, recall, mean average precision (mAP), and F1-score. These metrics are commonly used for object detection and segmentation tasks, and they are calculated based on the number of true positive (TP), true negative (TN), false positive (FP), and false negative (FN) predictions made by the model.

4.2.1 Intersection over Union (IoU)

To assess the accuracy of object detection algorithms we use the Intersection over Union (IoU) metric. It measures how well the algorithm's predicted bounding box overlaps with the ground truth bounding box. To calculate IoU, we compare the area of overlap between the predicted bounding box (referred to as the "candidate" box) and the ground truth bounding box (referred to as the "ground truth" box) to their combined area. The formula for IoU is:

$$IoU = \frac{Area(C) \cap Area(G)}{Area(C) \cup Area(G)}$$

Here, C represents the candidate bounding box, and G represents the ground truth bounding box where the actual object is located. The IoU value ranges from 0 to 1, with a higher value indicating a better algorithm performance. A higher IoU signifies a smaller difference between the candidate and ground truth bounding boxes, which implies a more accurate object detection result.

4.2.2 Precision-Recall Curve

The Precision-Recall Curve (P-R Curve) is a graphical representation that illustrates the relationship between the recall and precision metrics. In this curve, the x-axis represents the recall values, while the y-axis represents the precision values. Each point on the curve corresponds to a specific threshold value used in the algorithm. The points are connected to form a curve that provides insights into the trade-off between recall and precision. To calculate the recall (R) and precision (P) values for each point on the curve, we use the following equations:

$$Precision = \frac{TP}{(TP + FP)}$$
$$Recall = \frac{TP}{(TP + FN)}$$

By analyzing the P-R Curve, we can gain insights into the trade-off between precision and recall at different threshold values, helping us understand the performance of an algorithm in segmentation tasks.

4.2.3 F1-score

With the F1-score we can assess the accuracy of the models, providing a balanced evaluation by considering both precision and recall. It represents the harmonic mean of precision and recall and is defined as,

$$F1 - score = \frac{2PR}{(P + R)} = \frac{2TP}{(2TP + FP + FN)}.$$

In short, the F1-score combines both precision and recall giving a single value that represents the algorithm's overall accuracy. A higher F1-score indicates a better algorithm performance in achieving both high precision and high recall simultaneously.

4.2.4 Mean Average Precision (mAP)

Mean Average Precision (mAP) is a widely adopted evaluation metric for assessing the performance of object detection algorithms across multiple classes. In this paper, we considered mAP 50 and mAP 50-95, in which, mAP 50 calculates the average precision for all classes at an IoU threshold of 0.5 while mAP 50-95 computes the average precision for all classes over a range of IoU thresholds from 0.5 to 0.95, with a step size of 0.05. This variation of mAP offers a more comprehensive evaluation by considering a wider range of IoU thresholds.

5 Result and Discussion

5.1 Model Selection

In this work, we have used the pre-trained yolov8 for fiber and vessel detection as well as segmentation. We have used 3 YOLO variants m, l, and x with our custom dataset. YOLOv8-m used a medium-sized feature extractor, YOLOv8-l utilized a larger feature extractor compared to YOLOv8-m, and YOLOv8-x used an even larger feature extractor and more feature fusion compared to YOLOv8-l. The quantitative results for precision, recall, F1 score, mAP@0.5, and mAP@0.5-0.95 values of the three YOLOv8 models in fiber and vessel segmentation are presented in Table 2. Among these models, YOLOv8m-seg demonstrated the highest precision (0.97), recall (0.91), and F1 score (0.94), while performing relatively lower in mAP: 0.5-0.95 (0.75). YOLOv8l-seg outperformed YOLOv8m-seg only in mAP: 0.5-0.95 (0.76).

Based on these findings, the YOLOv8x-seg model was identified as the optimal choice for fiber and vessel detection and segmentation, exhibiting superior performance across the evaluation metrics of mAP@0.5 and mAP@0.95. Consequently, the YOLOv8x-seg model was selected for further analysis, specifically in estimating fiber and vessel length, width, and area. This selection ensures a consistent and focused evaluation of the model’s practical application, aligning with the study’s objectives.

Table 2 The table shows results for detecting fibers and vessels using YOLOv8 models. PARAM(M) is a trainable parameter in the model.

Model	Precision	Recall	F1-Score	mAP 50	mAP 50-95	Param (M)
YOLOv8m-seg	0.97	0.91	0.94	0.95	0.75	27.2
YOLOv8l-seg	0.96	0.91	0.94	0.94	0.76	45.9
YOLOv8x-seg	0.97	0.90	0.93	0.95	0.78	70.1

5.2 Model Performance

We thoroughly evaluated model performance for the tasks of detecting and segmenting fiber and vessel objects in images. We examined precision-recall curves to understand the trade-off between precision and recall for detection. For segmentation, we focused on how precisely the model delineates the boundaries and segments of the detected objects. Additionally, we analyzed F1-confidence curves to understand the relationship

between F1 scores and model confidence levels for detection and segmentation. Examining the F1-confidence curves provided insights into how precision and recall were balanced across varying confidence thresholds. Evaluating the model’s performance step-by-step is important for assessing its effectiveness.

Figure 3 depicts the behavior of the selected yolov8x-seg model used for object detection and segmentation of fiber and vessel objects. The precision-recall curve in Fig. 3(a) represents the trade-off between precision and recall for the detection task. At a threshold of 0.5, the mean average precision (mAP) values were 0.951 for fiber and 0.959 for vessel detection. The overall mAP of 0.955 for all classes combined indicated the model’s overall performance in object detection.

Figure 3(b) shows the F1-confidence curve, which illustrates the relationship between the F1 score and the model’s confidence. At a confidence threshold of 0, the F1-score was 0.95 for both fiber and vessel classes. This score represents the balance between precision and recall. A higher F1-score indicates better model performance in terms of both precision and recall. These findings provide valuable insights into the model’s performance and help assess its suitability for detecting fiber and vessel objects in images.

Moving on to the segmentation task, the model achieved values of 0.942 and 0.959 at a threshold of 0.5 for fiber and vessel segmentation, respectively. The overall mAP of 0.95 for all combined classes at the same threshold is shown in Fig. 3(c), highlighting the model’s effectiveness in segmenting objects. Figure 3(d) displays the F1-confidence curve for the segmentation task, where the model attained an F1-score of 0.94 at a confidence threshold of 0. This score represents the trade-off between precision and recall for both fiber and vessel classes.

We conclude that for fiber and vessel detection and segmentation, the YOLOv8x-seg model performed best compared to other models in terms of mAP. The YOLOv8m-seg model had the lowest mAP value specifically for fiber detection and segmentation. It is worth noting that the task of segmenting fibers and vessels is quite challenging due to the overlap of objects in the images.

5.3 Qualitative Results

Figure 4 shows fiber and vessel detection and segmentation examples achieved using the YOLOv8x-seg model. These examples highlight the model’s ability to accurately identify and outline fiber and vessel structures in the images. The visual results obtained from the model not only demonstrate its potential within the scope of our study but also provide valuable insight into its practical application for fiber and vessel analysis.

We highlight that we conducted experiments using various background images. Still, the model successfully detected and segmented the fiber and vessel structures despite the differences in the image backgrounds. This highlights the effectiveness of the model, as it can perform well regardless of the background variations. Such robustness is particularly valuable in fiber and vessel segmentation, where images with diverse backgrounds are encountered.

Based on the findings of this study, we conclude that the YOLOv8 model family effectively detects and segments fibers and vessels in microscopy images. Despite

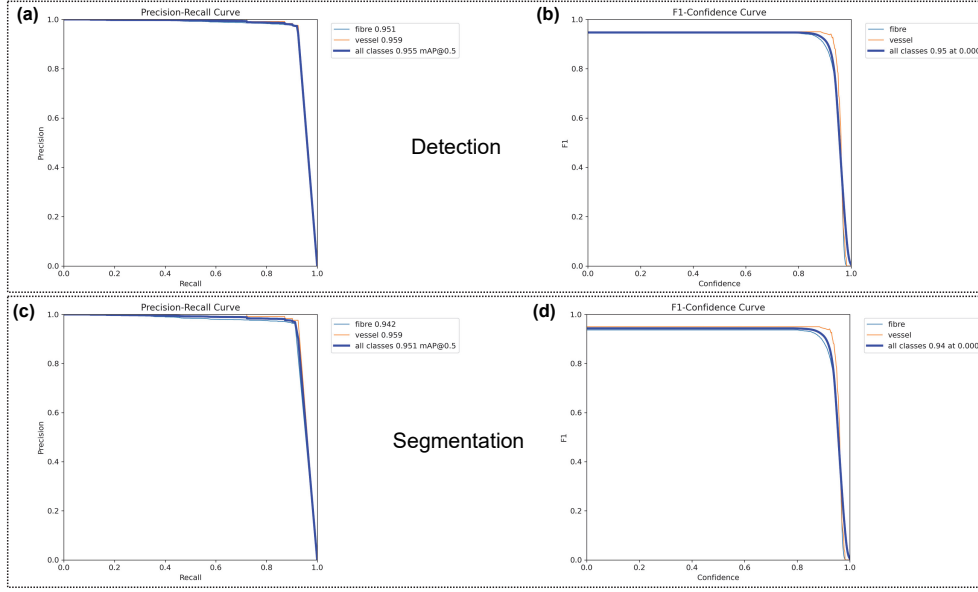


Fig. 3 These plots showcase the precision-recall and F1-confidence curves used to evaluate the performance of YOLOv8x in detecting and segmenting fibers and vessels. The model demonstrates strong mAP and F1-score across thresholds, confirming its effectiveness in object detection and segmentation tasks.

achieving high accuracy in fiber detection and segmentation, the YOLOv8 model still made some mistakes by generating false positives and false negatives in certain cases. We highly examples of this in Fig. 5 (a), where the model failed to identify a fiber segment, as highlighted by the yellow ellipse. This failure to detect the fiber was likely due to limitations in the training of the model. Similarly, in Fig. 5(b), the ellipse region highlights where YOLOv8 failed to identify the fiber and vessel. This is mainly because the number of samples used in this study for training the model is limited. To tackle this issue, Adar et al. [42] suggested that training the model with a larger dataset containing more input features can greatly enhance its ability to generalize and perform well on new and unseen data. A larger dataset would enable the model to capture the subtle differences in fiber and vessel structures in various background images. Additionally, a larger dataset can help to mitigate the risk of overfitting, where the model becomes too specialized to the training dataset and performs poorly on new samples.

5.4 Quantifying fibers and vessel in microscopy images

In order to complete the task of fiber and vessel detection and segmentation, we implemented standard measurements to describe the shape of the objects using the model output. Specifically, we evaluated how well our model performed with images of different sizes. We separated the images into two categories based on size. The first type measured 1920 x 1440 pixels and was used to train the model. The second type was a large image of 33 384 x 25 112 pixels stitched from 361 small 1920 x 1440 images. The

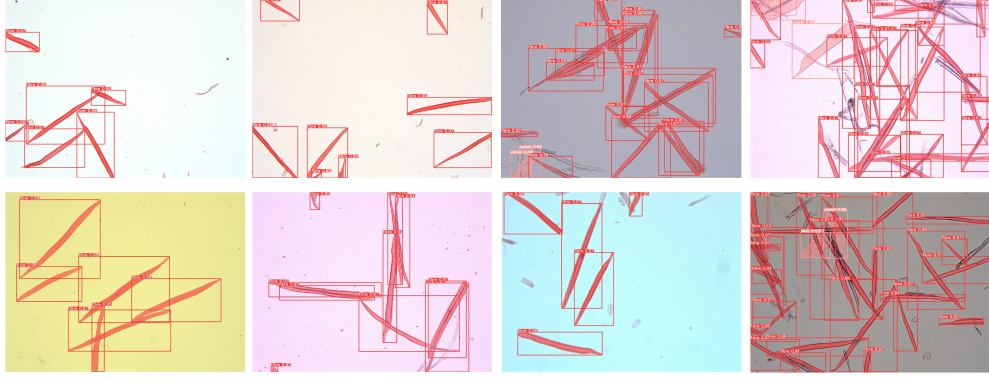


Fig. 4 The images depict YOLOv8 effectively detecting and segmenting variously shaped and sized fibers and vessels against diverse backgrounds, showcasing its robust performance across different scenarios.

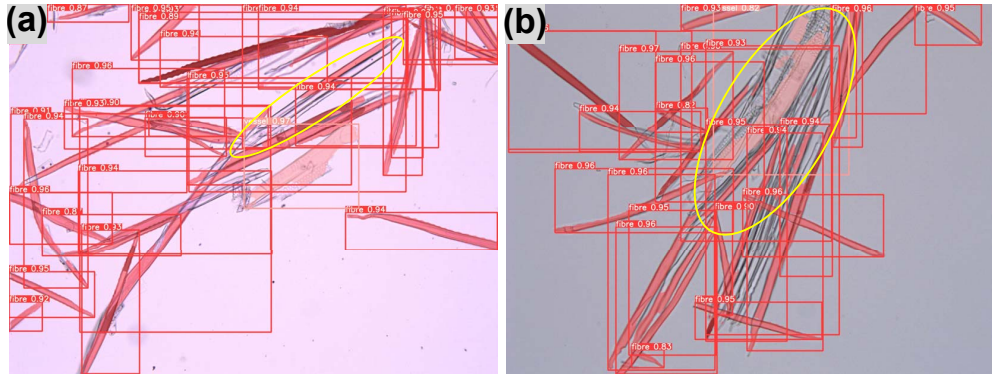


Fig. 5 The detection of fibers and vessels encountered some challenges, as shown in these examples where (a) a fiber was not detected, and (b) both a fiber and a vessel were not detected.

model first identified the locations of fibers and vessels in the image and then measured the morphological traits of the detected objects using the method described in subsection 3.3. For both image types, we used the trained model to measure characteristics like the length, width and area of the fibers and vessels detected. The total detected items in two large images are 1678 fibers and 117 vessels.

Figure 6 shows box plots summarizing the measurements of the detected fibers and vessels. For most fibers, the length ranged from 250-450 μm , the width ranged from 20-30 μm , and the area ranged from 6000-11 000 μm^2 . The average fiber length was 350 μm , the average width was 24 μm , and the average area was 8,561 μm^2 .

For most vessels, the length ranged from 220-270 μm , the average width ranged from 42-68 μm , and the area ranged from 10 000-22 000 μm^2 . The average vessel length was 280 μm , the average width was 56 μm , and the average area was 16 354 μm^2 . In the supplementary materials, scattered and histogram plots offer a detailed

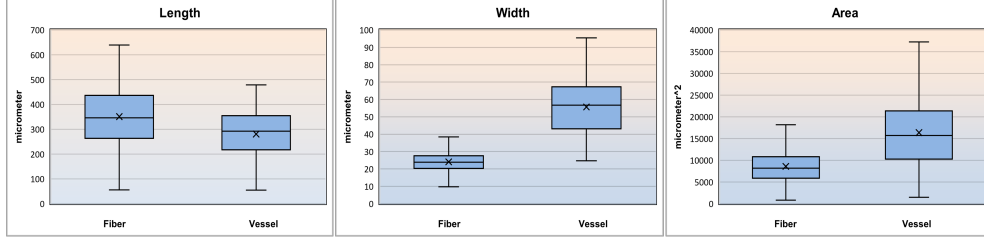


Fig. 6 Boxplots depict fibers' and vessels' length, width, and area measurements from two large images of 33,384 x 25,112 pixels. Fibers range from 250-450 μm long, 20-30 μm wide, and 6000-11 000 μm^2 in area. Vessels are 220-270 μm long, 42-68 μm wide, and 10 000-22 000 μm^2 in area. The box plots show the 1st and 3rd quartiles (box limits), mean values (cross sign), and median values (solid line).

visualization of the distribution and relationship between the length, width, and area in the image, as depicted in Fig. S3.

Further, testing on different image sizes allowed us to check if the model performance stayed consistent regardless of size changes. The results show that the model's effectiveness is independent of image dimensions. This scale-invariance makes the model more robust and can analyze images of varying sizes which are encountered in real applications. This property is crucial for real-world problems, as different image dimensions will inevitably be encountered in practice. To evaluate scale invariance and object detection and segmentation abilities, including overlapped objects, 20 small images of size 1920 x 1440 pixels were randomly selected, containing 137 fibers and 20 vessels. Measurements were compared to those from the large 33 384 x 25 112 pixel image.

We found the model extracted aligned average dimensions for fibers across these two image sizes in which overlapped fibers were also detected. This includes a length of $\approx 350 \mu\text{m}$, width of $\approx 25 \mu\text{m}$, and area of $\approx 9000 \mu\text{m}^2$ for the fibers. For fiber length, width, and area, the p-values were 0.964, 0.998, and 0.975, respectively, indicating no statistically significant difference between small and large image measurements. However, we noted a variability when comparing the vessel measurements with a lower average length of 248 μm and, higher average width of 65 μm . The vessel area averages were closer between image sizes at 16 556 μm^2 on small images and 16 892 μm^2 on large images. The p-values for vessel length, width, and area were 0.299, 0.124, and 0.413, respectively. These results illustrate the scale invariance performance of the model across different image dimensions. In the supplementary material, we also provide the analysis of 20 small-sized images (1920 x 1440), see Fig. S4 and two mid-sized images consisting of 99 tiles (8275 x 7250), see Fig. S5, using box plots, scatter plots, and histogram plots to assess the robustness of the model.

In conclusion, the capability to reliably extract metrics for fibers and vessels including overlapped at different scales highlights this model's strength in handling overlapping objects and scale invariance. These abilities are crucial for real-world applications requiring robust detection and segmentation alongside invariant performance across image sizes.

5.5 Comparison of GA20ox 1A line and wildtype T89

To further evaluate our approach for research applications, we tested it on a new dataset consisting of 12 large images of samples taken from the T89 wildtype tree and 12 large images from the transgenic line overexpressing the *GA20ox1* gene. This transgenic line was previously reported to show approximately 10 % increase in fiber length compared to the wildtype T89 [5]. In total, the model identified 5651 fibers in the 12 T89 images with an average length of $305.26 \pm 111 \mu m$ and for the GA20 line it identified 5782 fibers with an average of $354.30 \pm 78 \mu m$, see Fig. 7. A student t-test indicated that the samples were highly significant different, as evidenced by a p-value less than 0.0001. These results show an approximately 15 % length increase for the GA20ox line compared to the wildtype, in line with previously reported results.

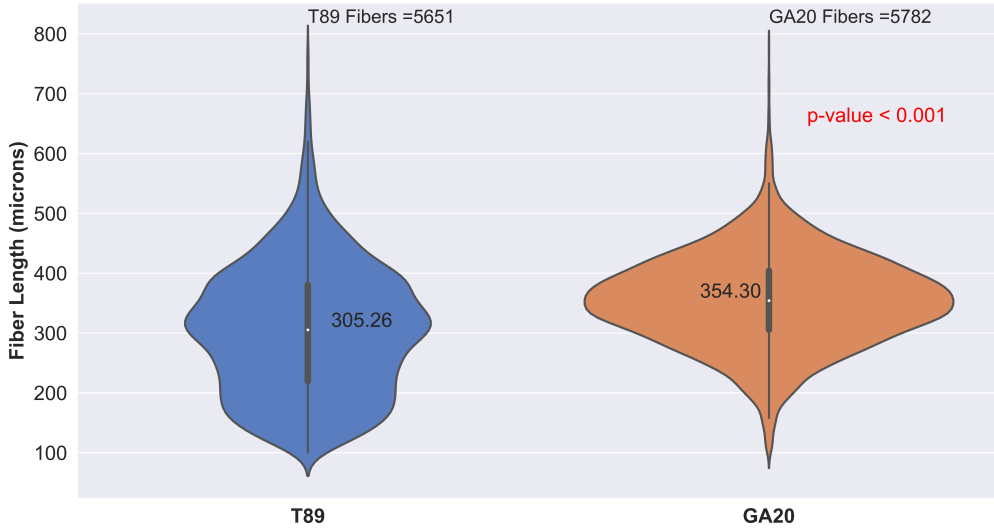


Fig. 7 Violin plots that depict fibers' length measurements from large images of 33 384 x 25 112 pixels from T89 and GA20ox line. The envelope shows the distribution, the thick center lines represent the 1st and 3rd quartiles (black line limits), and median values (center yellow dots).

5.6 GUI application

We have developed a desktop application using Python's Flask framework, designed to simplify the process of uploading and analyzing images with our automated algorithm. The application's workflow is shown in Fig. S6. Users can select an image from a gallery or upload one via drag-and-drop. Once an image is uploaded, the application predicts the presence of fibers and vessels. It also quantifies each detected object, with results available in a downloadable data file. This file includes details like object type, length, width, and area. When installed on a local computer with an i9 10th Gen processor and 32GB of RAM, the application processes a 1024 x 1024 image in an average of 140 milliseconds.

5.6.1 Github resources

Detailed instructions for installation of the developed code and instructions for implementation are found in the supporting information. Additionally, users can find instructions on how to retrain and test the model using Google colab in the GitHub resources [38]. The 'Train_custom_data.ipynb' file can be used to retrain the model; simply follow the instructions provided in the file. The 'prediction_file.ipynb' file is used to test the model on your custom dataset.

6 Conclusion

This paper introduces a deep learning solution using YOLOv8 to automatically analyze and quantify wood fibers and vessels in challenging microscope images, offering high-throughput capabilities. To achieve this, we trained multiple YOLOv8 models on diverse wood image datasets and evaluated their performance in detecting and segmenting fibers and vessels. The most robust model was chosen. The model can consistently and reliably extract essential cell metrics across different image scales, such as length, width, and area. The model's consistent metric extraction underscores its strong practical applicability. We also created a web application pipeline that is useful in practical situations. Users can then upload images for automatic cell counting and extraction. Thus, we conclude that this study introduces an innovative high-throughput method for analyzing wood cells in densely populated 2D microscopy images, even when cells are partially obscured.

Supplementary information. Additional information and user guides are included in the supporting information file.

Declarations

Funding

The project was funded by Kempestiftelserna (JCK-2129.3) and the National Academic Infrastructure for Supercomputing in Sweden (NAISS) at Umeå, partially funded by Vetenskapsrådet (2022-06725). The authors acknowledge the facilities and technical assistance of the Umeå Plant Science Centre Microscopy facility and the plant growth facility. This work was also supported by grants from the Wallenberg Foundation (KAW 2016.0341 and KAW 2016.0352), VINNOVA (2016-00504), and the Novo Nordisk Foundation (NNF21OC0067282) to S.V. We also thank Bio4Energy for supporting this work.

Declaration of competing interest

The authors declare that they have no known competing financial interests or personal relationships that could have appeared to influence the work reported in this paper.

Consent for publication

The authors declare that they have no competing interests.

Availability of data and code

All the code in this project was developed using python and different public libraries as defined in the supporting information. The Google Colab project is found here [37] and the code can be downloaded at a public GitHub repository here [38].

Authors' contributions

Saqib Qamar: Data curation, Software, Methodology, Validation, Formal analysis. Abu Imran Baba: Investigation, Validation. Stéphane Verge: Conceptualization, Resources, Supervision. Magnus Andersson: Conceptualization, Resources, Supervision, Funding acquisition, Project administration. All authors contributed to Writing, review and editing.

Ethics approval and consent to participate

No applicable

References

- [1] T. Gorshkova, N. Brutch, B. Chabbert, M. Deyholos, T. Hayashi, S. Lev-Yadun, E.J. Mellerowicz, C. Morvan, G. Neutelings, G. Pilate, Plant fiber formation: state of the art, recent and expected progress, and open questions. *Critical Reviews in Plant Sciences* **31**(3), 201–228 (2012)
- [2] K. Wilson, D.J.B. White, et al., *The anatomy of wood: its diversity and variability*. (Stobart & Son Ltd., 1986)
- [3] A. Siedlecka, S. Wiklund, M.A. Péronne, F. Micheli, J. Leśniewska, I. Sethson, U. Edlund, L. Richard, B. Sundberg, E.J. Mellerowicz, Pectin methyl esterase inhibits intrusive and symplastic cell growth in developing wood cells of populus. *Plant physiology* **146**(2), 554 (2008)
- [4] C. Schneider, W. Rasband, K.W. Eliceiri, Nih image to imagej: 25 years of image analysis. *Nature methods* **9**(7), 671–675 (2012)
- [5] M. Eriksson, M. Israelsson, O. Olsson, T. Moritz, Increased gibberellin biosynthesis in transgenic trees promotes growth, biomass production and xylem fiber length. *Nature biotechnology* **18**(7), 784–788 (2000)
- [6] P. Kennel, G. Subsol, M. Guérout, P. Borianne, *Automatic identification of cell files in light microscopic images of conifer wood*, in *2010 2nd international conference on image processing theory, tools and applications* (IEEE, 2010), pp. 98–103
- [7] M. Aronsson, *On 3D fibre measurements of digitized paper*, vol. 254 (2002)

- [8] M. Donoser, H. Riemenschneider, H. Bischof, *Efficient partial shape matching of outer contours*, in *Computer Vision-ACCV 2009: 9th Asian Conference on Computer Vision, Xi'an, September 23-27, 2009, Revised Selected Papers, Part I 9* (Springer, 2010), pp. 281–292
- [9] C. Lu, L.J. Latecki, N. Adluru, X. Yang, H. Ling, *Shape guided contour grouping with particle filters*, in *2009 IEEE 12th International Conference on Computer Vision* (IEEE, 2009), pp. 2288–2295
- [10] S. Pan, M. Kudo, Recognition of wood porosity based on direction insensitive feature sets. *Trans. Mach. Learn. Data Min.* **5**(1), 45–62 (2012)
- [11] G. Brunel, P. Borianne, G. Subsol, M. Jaeger, Y. Caraglio, Automatic identification and characterization of radial files in light microscopy images of wood. *Annals of botany* **114**(4), 829–840 (2014)
- [12] H. Boztoprak, M. Ergun, Determination of vessel and fibers in hardwoods. *Gaziosmanpasa Journal of Scientific Research* **6**(2), 87–96 (2017)
- [13] A. Voulodimos, N. Doulamis, A. Doulamis, E. Protopapadakis, et al., Deep learning for computer vision: A brief review. *Computational intelligence and neuroscience* **2018** (2018)
- [14] Z.Q. Zhao, P. Zheng, S.t. Xu, X. Wu, Object detection with deep learning: A review. *IEEE transactions on neural networks and learning systems* **30**(11), 3212–3232 (2019)
- [15] E. Cambria, B. White, Jumping nlp curves: A review of natural language processing research. *IEEE Computational intelligence magazine* **9**(2), 48–57 (2014)
- [16] M. Reichstein, G. Camps-Valls, B. Stevens, M. Jung, J. Denzler, N. Carvalhais, f. Prabhat, Deep learning and process understanding for data-driven earth system science. *Nature* **566**(7743), 195–204 (2019)
- [17] S. Qamar, H. Jin, R. Zheng, P. Ahmad, M. Usama, A variant form of 3d-unet for infant brain segmentation. *Future Generation Computer Systems* **108**, 613–623 (2020)
- [18] A. Vaswani, N. Shazeer, N. Parmar, J. Uszkoreit, L. Jones, A.N. Gomez, L. Kaiser, I. Polosukhin, Attention is all you need. *Advances in neural information processing systems* **30** (2017)
- [19] Y. LeCun, Y. Bengio, G. Hinton, Deep learning. *nature* **521**(7553), 436–444 (2015)

- [20] A. Biem, Neural networks: A review. Data classification: Algorithms and applications pp. 205–244 (2014)
- [21] S. Qamar, R. Öberg, D. Malyshev, M. Andersson, A hybrid cnn-random forest algorithm for bacterial spore segmentation and classification in tem images. *Scientific Reports* **13**(1), 18758 (2023)
- [22] J. Long, E. Shelhamer, T. Darrell, *Fully convolutional networks for semantic segmentation*, in *2015 IEEE Conference on Computer Vision and Pattern Recognition (CVPR)* (2015), pp. 3431–3440. <https://doi.org/10.1109/CVPR.2015.7298965>
- [23] V. Badrinarayanan, A. Kendall, R. Cipolla, Segnet: A deep convolutional encoder-decoder architecture for image segmentation. *IEEE transactions on pattern analysis and machine intelligence* **39**(12), 2481–2495 (2017)
- [24] O. Ronneberger, P. Fischer, T. Brox, *U-net: Convolutional networks for biomedical image segmentation*, in *Medical Image Computing and Computer-Assisted Intervention–MICCAI 2015: 18th International Conference, Munich, Germany, October 5–9, 2015, Proceedings, Part III 18* (Springer, 2015), pp. 234–241
- [25] H. Fu, Y. Xu, S. Lin, D.W. Kee Wong, J. Liu, *Deepvessel: Retinal vessel segmentation via deep learning and conditional random field*, in *Medical Image Computing and Computer-Assisted Intervention–MICCAI 2016: 19th International Conference, Athens, Greece, October 17–21, 2016, Proceedings, Part II 19* (Springer, 2016), pp. 132–139
- [26] S. Ren, K. He, R. Girshick, J. Sun, Faster r-cnn: Towards real-time object detection with region proposal networks. *Advances in neural information processing systems* **28** (2015)
- [27] K. He, G. Gkioxari, P. Dollár, R. Girshick, *Mask r-cnn*, in *Proceedings of the IEEE international conference on computer vision* (2017), pp. 2961–2969
- [28] T. Lin, P. Dollár, R. Girshick, K. He, B. Hariharan, S. Belongie, *Feature pyramid networks for object detection*, in *Proceedings of the IEEE conference on computer vision and pattern recognition* (2017), pp. 2117–2125
- [29] J. Johnson, Adapting mask-rcnn for automatic nucleus segmentation. *arXiv preprint arXiv:1805.00500* (2018)
- [30] H. Tsai, J. Gajda, T.F. Sloan, A. Rares, A.Q. Shen, Usiigaci: Instance-aware cell tracking in stain-free phase contrast microscopy enabled by machine learning. *SoftwareX* **9**, 230–237 (2019)
- [31] R. Hollandi, A. Szkalisity, T. Toth, E. Tasnadi, C. Molnar, B. Mathe, I. Grexa, J. Molnar, A. Balind, M. Gorbe, et al., A deep learning framework for nucleus

- segmentation using image style transfer. Biorxiv p. 580605 (2019)
- [32] K. Simonyan, A. Zisserman, Very deep convolutional networks for large-scale image recognition. arxiv 1409.1556 (09 2014). URL <https://arxiv.org/abs/1409.1556>. Accessed: February (2020)
 - [33] K. He, X. Zhang, S. Ren, J. Sun, *Deep residual learning for image recognition*, in *Proceedings of the IEEE conference on computer vision and pattern recognition* (2016), pp. 770–778
 - [34] A. Neubeck, L. Van Gool, *Efficient non-maximum suppression*, in *18th international conference on pattern recognition (ICPR'06)*, vol. 3 (IEEE, 2006), pp. 850–855
 - [35] W. Liu, D. Anguelov, D. Erhan, C. Szegedy, S. Reed, C.Y. Fu, A.C. Berg, *Ssd: Single shot multibox detector*, in *Computer Vision–ECCV 2016: 14th European Conference, Amsterdam, The Netherlands, October 11–14, 2016, Proceedings, Part I 14* (Springer, 2016), pp. 21–37
 - [36] G. Jocher, A. Chaurasia, J. Qiu. Ultralytics yolov8 (2023). URL <https://github.com/ultralytics/ultralytics>
 - [37] E. Bisong, *Google Colaboratory* (Apress, Berkeley, CA, 2019), pp. 59–64
 - [38] S. Qamar. fiberseg (2023). URL <https://github.com/sqbqamar/fiberseg>
 - [39] A. Dutta, A. Zisserman. The via annotation software for images, audio and video (2019)
 - [40] G. Bradski, The OpenCV Library. Dr. Dobb’s Journal of Software Tools (2000)
 - [41] J. Glenn. Yolov5 release v6. 1 (2022)
 - [42] M. Frid, E. Klang, M. Amitai, J. Goldberger, H. Greenspan, *Synthetic data augmentation using GAN for improved liver lesion classification*, in *2018 IEEE 15th International Symposium on Biomedical Imaging (ISBI 2018)* (2018), pp. 289–293. <https://doi.org/10.1109/ISBI.2018.8363576>